



Sensor fusion of two sonar devices for underwater 3D mapping with an AUV

Hangil Joe¹ · Hyeonwoo Cho² · Minsung Sung² · Jinwhan Kim³ · Son-cheol Yu²

Received: 13 June 2019 / Accepted: 10 May 2021 / Published online: 4 June 2021

© The Author(s), under exclusive licence to Springer Science+Business Media, LLC, part of Springer Nature 2021

Abstract

We present herein a three-dimensional (3D) mapping method in one-way rectilinear scanning with an autonomous underwater vehicle (AUV) equipped with a forward looking sonar (FLS) and a profiling sonar (PS). Three-dimensional reconstruction using sonar with a finite beam width is an ill-posed problem, and additional constraints also need to be considered. Our approach involves an additional sonar and fuse acoustic measurements provided by the two sonar sensors. The FLS has a high resolution in the horizontal scan but has a uncertainty in the vertical scan. Meanwhile, the PS provides a reliable vertical profile, but its beam width is extremely narrow. An initial map is generated by the FLS and refined by combining the PS vertical scan data. To demonstrate the validity and effectiveness of the proposed method, we conducted tests in a water tank and also at sea. Finally, we presented the results of the proposed method gathered by an AUV in the tests.

Keywords Sensor fusion · Autonomous underwater vehicle · 3D reconstruction · Underwater mapping · Forward looking sonar · Profiling sonar

1 Introduction

Autonomous underwater vehicles (AUVs) must perceive the surroundings and infer their current location on the basis of the perceived information for self-localization. Thus, reliable map generation based on perceived information should be performed before localization. As laser-based sensors cannot be easily used in water owing to their rapid light absorption,

sonar is a common solution employed for underwater mapping.

Sonar devices are robust to water turbidity and widely used for underwater sensing in limited visibility environments. Compared with laser-based sensors, the lack of information of sonar data is inevitable causing issues, such as loss of elevation information, perceptual ambiguity, and a high proportion of outliers (Hurtós 2014), which complicate sonar data processing and three-dimensional (3D) map building. 3D reconstruction is a conventional research topic explored in the field of underwater sonar; however, 3D mapping through sonars is considered challenging (VanMiddlesworth et al. 2015; Teixeira et al. 2016).

Several advanced studies have introduced various methods for map building through sonar. Early research involved two dimensional (2D) map building in man-made structured environments. Ribas et al. modeled sonar scans as geometric shapes such as a line and a rectangle, in a 2D horizontal plane (Ribas et al. 2006, 2010). This method can be used to scan a coastal environment with artificial structures. Other approaches compute the uncertainty of return data and build probabilistic pointclouds to overcome noisy sonar data (Hernández Bes et al. 2009; Burguera 2017). In some studies (Kim et al. 2004; Walter et al. 2008), researchers reconstructed elevation information from epipolar geometry by

✉ Son-cheol Yu
sncyu@postech.ac.kr

Hangil Joe
hgjoe@knu.ac.kr

Hyeonwoo Cho
lighto@postech.ac.kr

Minsung Sung
ms.sung@postech.ac.kr

Jinwhan Kim
jinwhan@kaist.ac.kr

¹ The Department of Robot and Smart System Engineering, Kyungpook National University, Daegu, Republic of Korea

² The Department of Creative IT Engineering, POSTECH, Pohang, Kyungbuk, Republic of Korea

³ The Department of Mechanical Engineering, KAIST, Daejeon, Republic of Korea

obtaining data from different points of view. Furthermore, high-frequency forward-looking sonar (FLS) has been used for 3D reconstruction. Aykin et al. reported 3D underwater object reconstruction with acoustic lens based forward scanning sonar through space carving (Aykin and Negahdaripour 2016), and Guerneve et al. presented a 3D reconstruction method using deconvolution and space carving with narrow-beam synthetic aperture sonar (SAS) (Guerneve et al. 2018). Because extracting 3D information from sonar images is an ill-posed problem, a sufficient number of sonar images must be acquired at various positions around an object of interest. For navigation-purposed mapping, the generation time to obtain sufficient data for extracting 3D information should be minimized; thus, a fly-by mission that deters a constrained hovering around an object of interest is required. Cho et al. proposed a pointclouds generating method using FLS (Cho et al. 2017) that uses successive sonar images obtained from a linearly moving AUV to extract the height information of a protruded object on a seabed. They used highlight variations on sonar images when an FLS-equipped AUV moved along the rectilinear trajectories, which is called a highlight extension. Unlike maps from echo sounders and side scan sonars, maps generated by high-frequency FLS are of high resolution and can identify small objects on a seabed (Belcher et al. 2002). However, the generated pointclouds show an erroneous pattern in the front area of the generated points of an object, which degrade the accuracy, especially for small objects. We called the erroneous pattern in the front area as the front slope.

In this study, we analyze the front slope and degradation of generated pointclouds in a one-way rectilinear scan and propose a refined method for seabed mapping. The conditions of the proposed method are as follows: (1) deterring circular hovering around an object of interest (one-way scan), (2) navigation-purpose 3D reconstruction, and (3) optimized solution for seabed tracking. To satisfy the conditions, we used two heterogeneous sonar devices. To reconstruct 3D information, an additional range with an incident angle is required. If the FLS is mounted on an AUV, then we can obtain the additional range and angle using the Doppler velocity log (DVL) as the altitude, which is presented in (Cho et al. 2017). If the additional information is extended, then an improved map can be obtained. In this context, we used an FLS and a profiling sonar (PS). Here, the generated map by the FLS that contains errors owing to the perceptual ambiguity is refined by combining the vertically scanned information from a PS. Upon comparison the two sonar sensors, it is observed that the FLS is an acoustic-lens-based high-resolution sonar, and provides a wider field of view (FOV) in the horizontal direction with a relatively short scanning range, whereas the PS has a narrow FOV with a medium scanning range. Through the installation of the PS on its side, the lay-down PS is obtained, which scans the vertical profiles

that are utilized to reconstruct the lost elevation information of data from the FLS. For the relevant point extraction of the FLS data, we used the highlight extension presented in Cho et al. (2017), and for sonar data processing, we divided the sonar data of the FLS into vertical sectional slices and extracted their line features. On the basis of the line features, the data from the two sonar sensors were matched with their correspondences. The proposed method was demonstrated in a tank test in which five different objects were installed and a seatrial, and the results were analyzed.

This paper is organized as follows. First, we present point-cloud generation using a single FLS in a fly-by mission. Then, we analyze the limitation of the method using a single FLS and define the front slope and degradation of the generated pointclouds. Subsequently, we present the pointcloud generation method through the fusion of two sonar sensors to mitigate the limitation. We apply the proposed method to an AUV and demonstrated it through experiments in an indoor water tank and the sea. Finally, we present the conclusions.

2 Pointcloud generation using a single sonar

For reconstruction of the 3D information using a single sonar, an additional range and the incident angle are required. In AUV applications, the additional range is replaced by the altitude from the DVL, and the incident angle is perpendicular to the seabed. With the additional information, the FLS on the moving AUV can estimate the height of the object. This section addresses the pointcloud generation method using a single sonar and analyzes the limits of the single-sonar method.

2.1 Sonar configuration

The FLS we used comprises 96 transducers, each having a fan-shaped acoustic beam spreading angle of 0.3° (horizontal) and of 14° (vertical) (Belcher et al. 2002). The vertical view of the acoustic beam geometry of the FLS is shown in Fig. 1, and its horizontal view is presented in Fig. 2a. The transducer array emits 12 acoustic beams in 8 transmit-receive cycles to prevent interference. For a 10 m scanning range, a period of 100 ms is required to obtain the entire return data that are synthesized into a 512×96 image as shown in Fig. 2b. r_{min} and r_{max} represent the actual FOV of sonar determined by the acoustic beam shape, and s is the vertical beam spreading angle. r_{min} and r_{max} are the user-defined window sizes that determine the minimum and maximum ranges of the resulting sonar image, respectively. t is the sonar tilt angle, and h_r is the altitude of the sonar. r_c is a return beam that is mapped into a sonar image on the basis of the time of flight and returning intensity from the sonar to the object.

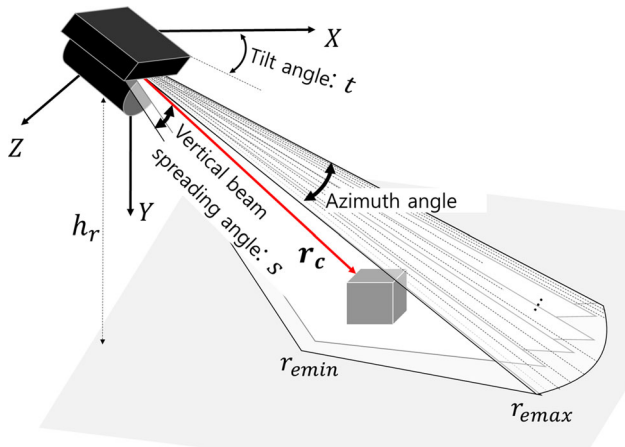


Fig. 1 Acoustic beam geometry of the FLS in the vertical view

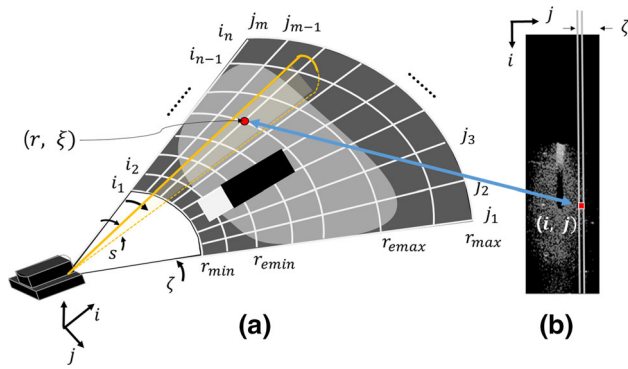


Fig. 2 Acoustic beam geometry of the FLS in the horizontal view. **a** horizontal view of the acoustic geometry of the FLS, **b** resulting raw acoustic image

2.2 Point cloud generation using FLS

Let the sonar return data be $I(i, j)$, and let the i -th row of $I(i, j)$ be $I_r(i)$, where $i = \{1 \dots n\}$ and $j = \{1 \dots m\}$. First, the sonar images are divided into two areas: effective and front areas. They are divided by r_{min} and r_{max} :

$$r_{min} = \frac{h_r}{\sin(t(\zeta) + s/2)}, \quad I_{min} = \left[n \frac{r_{min} - r_{min}}{r_{max} - r_{min}} \right], \quad (1)$$

$$r_{max} = \frac{h_r}{\sin(t(\zeta) - s/2)}, \quad I_{max} = \left[n \frac{r_{max} - r_{min}}{r_{max} - r_{min}} \right], \quad (2)$$

where t and s are the tilt angle of the sonar and the vertical beam spreading angle, respectively. ζ is the azimuth angle, where $-14.5 < \zeta < 14.5$, and $[\cdot]$ is the nearest integer function. r_{min} and r_{max} represent the lower and upper boundaries of the FOV of FLS (Fig. 1), respectively, and I_{min} and I_{max} denote the pixel indices corresponding to r_{min} and r_{max} , respectively, as shown in Fig. 4. On the basis of I_{min}

and I_{max} , the effective and front areas are defined as follows

$$\text{Front area } S : \text{set } I_r(i) \in S(i, j) \text{ that } I_r(i) \leq I_{min}, \quad (3)$$

$$\text{Effective area } E : \text{set } I_r(i) \in E(i, j) \text{ that } I_r(i) > I_{min} \quad (4)$$

$$\text{and } I_r(i) \leq I_{max}. \quad (5)$$

The effective area is the FOV of the sonar, and the front area in the sonar image is a closer area exceeding the front side of the effective area. If a protruded object exists on the seabed in the FOV of the sonar exceeding r_{min} over the front-top part of the object, then the front-top part of the object maps a highlighted region on the front area in the sonar image (Fig. 3). The highlighted region on the front area in the sonar image, called the highlight extension effect (HEE) is key to the extraction of the height information from the 2D sonar image. A stepwise variation of a sonar image, where the AUV-equipped FLS is assumed to move forward, is presented in Fig. 4. As the AUV approaches an object with a constant altitude, the length of the highlight extension reaches a certain value, called the critical point. At the critical point, the length of the highlight extension no longer increases, and the critical point depends on the height of the object. The beam geometry of the FLS and the critical point can be used to estimate the height of the object. The frontmost edge in the highlighted region can be obtained via intensity difference filtering after Gaussian filtering on the front area in the sonar image $S(i, j)$.

$$\mathbf{S}_G(i, j) = \sum_{k=-2}^2 \mathbf{S}(i+k, j) \mathbf{G}(k, j), \quad (6)$$

$$\mathbf{S}_D(i, j) = \sum_{k=-1}^1 \mathbf{S}_G(i+k, j) \mathbf{D}(k, j), \quad (7)$$

where

$$\mathbf{G} = [\bar{\mathbf{g}}_1(x; \sigma), \dots, \bar{\mathbf{g}}_m(x; \sigma)], \quad (8)$$

$$\bar{\mathbf{g}}_i(x; \sigma) = \frac{1}{\sqrt{2\pi}\sigma} \exp\left(-\frac{x^2}{2\sigma^2}\right) : \mathbf{x} = [-2, -1, 0, 1, 2]^T, \quad (9)$$

$$\bar{\mathbf{g}}_i(x; \sigma) = \mathbf{g}_i(x; \sigma) / \sum_{k=-2}^2 \mathbf{g}_i(k; \sigma), \quad (10)$$

$$\mathbf{D} = \begin{bmatrix} -1 & \dots & -1 \\ 0 & \ddots & 0 \\ 1 & \dots & 1 \end{bmatrix}_{3 \times m}. \quad (11)$$

The vector of the pixel indices of the critical points, $I_c(j)$, is calculated by extracting the maximum values in each column

Fig. 3 Highlighted region of an object is extended when an AUV approaches an aluminum cylinder. Frames **a–f** in this figure correspond to **a–f** in Fig. 4, respectively

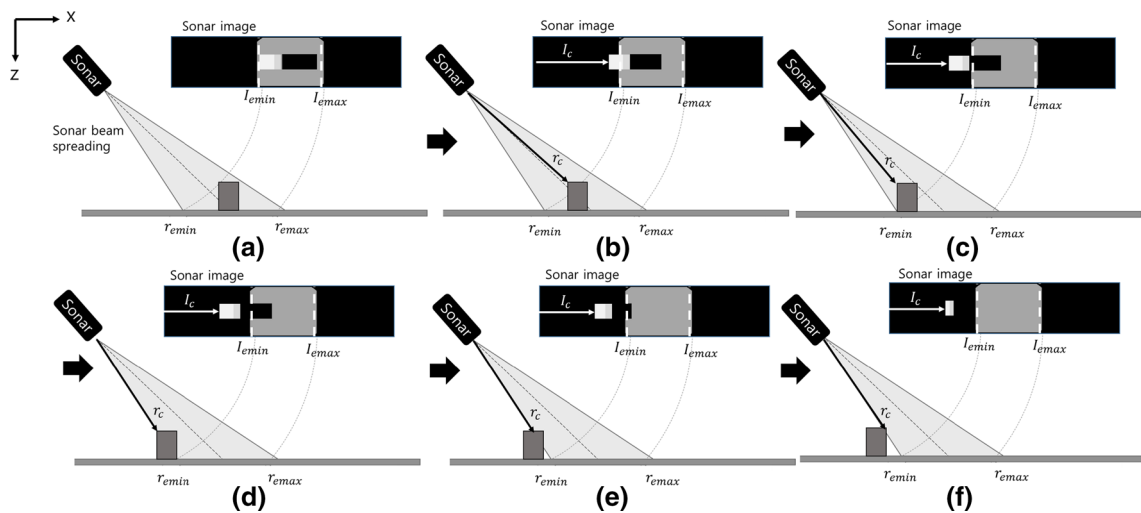
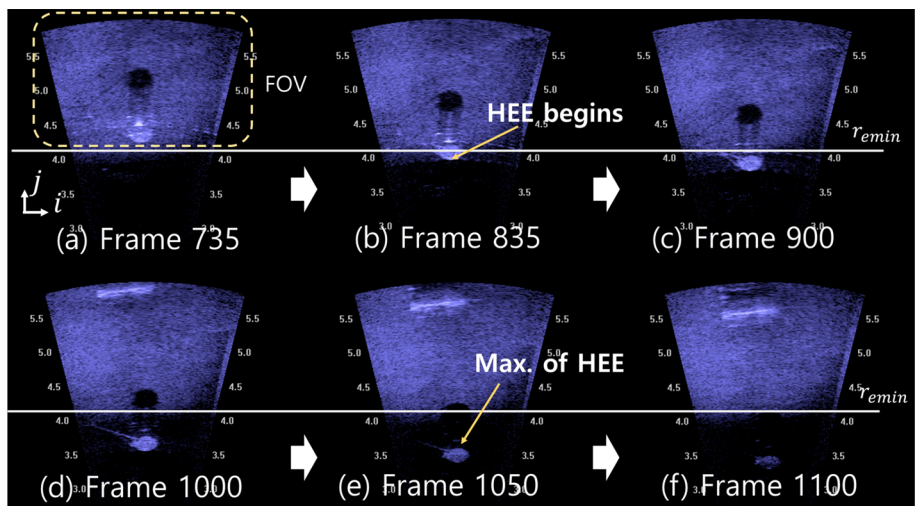


Fig. 4 Stepwise change in the length of highlight in the front area in a sonar image when the position of sonar changes forwardly from **a–f**

on $\mathbf{S}_D(i, j)$ as follows:

$$I_c(j) = \operatorname{argmax}_i \mathbf{S}_D(i, j). \quad (12)$$

The distance from the critical points to the FLS is

$$r_c(j) = r_{min} + (r_{max} - r_{min}) \frac{I_c(j)}{n}. \quad (13)$$

Let the AUV position be $\mathbf{x}_r = [x_r, y_r, z_r]^T$. Subsequently, the point of the object, $\mathbf{P}_t = [\mathbf{x}_t, \mathbf{y}_t, \mathbf{z}_t]^T$, can be obtained as follows:

$$\mathbf{P}_t(j) = \mathbf{x}_r + r_c(j) \mathbf{T}(t, s, \theta_r, \zeta, \psi_r) \quad (14)$$

where θ_r, ψ_r are the roll, pitch and yaw of the AUV, respectively,

$$\mathbf{T}(t, s, \theta_r, \zeta, \psi_r) \quad (15)$$

$$= \begin{bmatrix} \sqrt{1 - \sin^2(t(\zeta) + s/2 + \theta_r) - \sin^2(\zeta + \psi_r)} \\ \sin(\zeta + \psi_r) \\ -\sin(t(\zeta) + s/2 + \theta_r) \end{bmatrix}$$

2.3 Disadvantages of the single-sonar method

As the FLS provides high-resolution sonar images, the method above allows for the recognition of a small object (<10 cm) on the seabed. In addition, the method is simple, so it can be utilized for online map building. However, the loss of elevation information is the indisputable disadvantage in reconstructing 3D information from a 2D sonar image, and the generated pointclouds using a single sonar accompany uncertainties and errors. The most crucial error is the slope in front of the generated points of a protruded object (Fig. 5), which is caused by an ambiguous state before the critical point is reached.

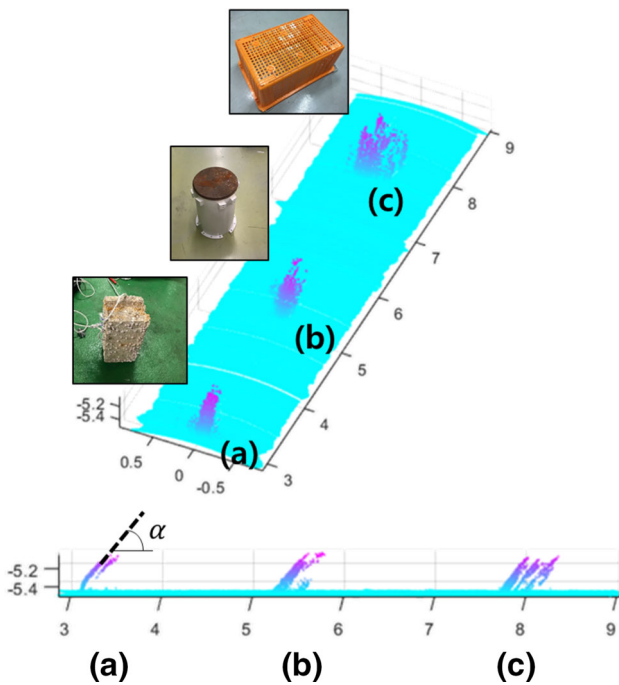


Fig. 5 Generated point and undesired slope in front of the points

When the AUV begins to approach a protruded object, the upper boundary r_{emax} of the FOV of the sonar passes through the front area of the object. Figure 4 describes the change in the sonar image as the AUV approaches the object during a fly-by mission. As the AUV approaches the object more, the distance from the sonar to the frontmost edge of the object becomes closer than that of the lower boundary r_{emin} , where the highlight extension begins. From this moment, as shown in Fig. 4a–c, the closer the AUV approaches, the longer the highlight is in the front area. When the lower boundary of the FOV is about to pass through the object (Fig. 4d), the length of the highlight in the front area in the sonar image no longer increases, and is maintained constant until the object completely passes through the lower boundary of the sonar FOV (Fig. 4 e, f). This point (moment) is called the critical point, at which the highlight in the front area in the sonar image attains the maximum value, and the height, h , of the object is derived from the maximum length of the highlight using Eq. 16. Before the (d) moment is reached, (b) and (c) are transient stages, where the exact height of the object cannot be calculated; these moments are termed as the ambiguous stages. Without prior information, we cannot determine the exact moment of the critical point (d), which results in the front slope in the generated pointclouds.

$$h = h_r - r_c \sin(t(\zeta) + s/2) \quad (16)$$

The front slope can be modeled. Given that the elevation angle is sufficiently narrow, the geometry of the sonar can be

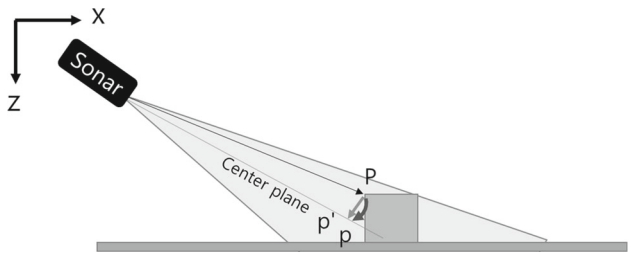


Fig. 6 Orthographic projection approximation. p is the original point of P mapped by sonar geometry, and p' is the projected point of P on the center plane of the acoustic beam

described as an orthographic camera (Walter 2008), which is called orthographic projection approximation. An acoustic signal reflected from a point P on an object is mapped into point p in the resulting image plane along the arc defined by the corresponding elevation angle and distance. Under the orthogonal approximation, the point P is mapped into p' that is a projected point. This process is equivalent to P being projected onto the center plane (Fig. 6) (Hurtós 2014).

When the AUV moves from $x_{r,t}$ to $x_{r,t+1}$, the length of the highlight in the image plane increases from $I_{c,t}$ to $I_{c,t+1}$ (Fig. 7a). On the basis of the sonar projection geometry, $I_{c,t}$ is approximated as $r_{emin} - T_t$ (Fig. 7), where T_t is the distance to the frontmost edge of an object from r_{emin} at time t , and T_{t+1} is obtained using $T_t + (x_{r,t+1} - x_{r,t}) \cos(t)$. The variation $T_{t+1} - T_t$ is denoted by $\Delta T = (x_{r,t+1} - x_{r,t}) \cos(t) = \Delta x \cos(t)$, and the variation $I_{c,t+1} - I_{c,t}$ is represented by $\Delta I_c = -\Delta T$.

The slope of the points can be derived in the pointcloud map M , t. The derivatives between the generated points in the X-Z plane are as follows:

$$\begin{aligned} \Delta \mathbf{x}_t(j) &= \Delta x_r \\ &+ \Delta r_c(j) \sqrt{1 - \sin^2(t + s/2 + \theta_r) - \sin^2(\zeta + \psi_r)}, \end{aligned} \quad (17)$$

$$\Delta \mathbf{z}_t(j) = \Delta z_r - \Delta r_c(j) \sin(t(\zeta) + s/2 + \theta_r), \quad (18)$$

where $\Delta r_c \approx -\Delta x_r \cos(t(\zeta) + \theta_r)$, and z_r is constant. Accordingly, the slope is obtained as follows:

$$\begin{aligned} \Delta \mathbf{x}_r(j) &= \Delta x_r (1 - \cos(t(\zeta) + \theta_r) \cos(t(\zeta) + s/2 + \theta_r)), \\ &\quad (19) \end{aligned}$$

$$\Delta \mathbf{z}_r(j) = \Delta x_r \cos(t(\zeta) + \theta_r) \sin(t(\zeta) + s/2 + \theta_r), \quad (20)$$

$$\alpha(j) = \tan^{-1}\left(\frac{\cos(t(\zeta) + \theta_r) \sin(t(\zeta) + s/2 + \theta_r)}{1 - \cos(t(\zeta) + \theta_r) \cos(t(\zeta) + s/2 + \theta_r)}\right). \quad (21)$$

As represented in Eq. 21, the slope of points \mathbf{P}_t is determined by the predetermined values including the tilt angle

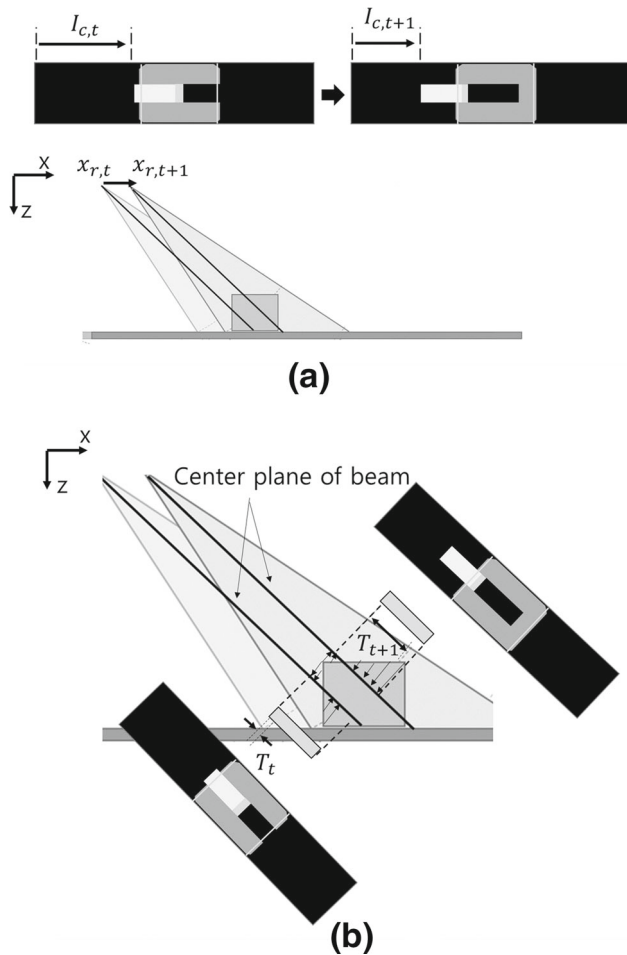


Fig. 7 Change in length of the highlight in the front area in the sonar image with change in sonar position

Table 1 Comparison of the predicted slope and real slope in the experiment

Sonar configuration	Predicted slope	Experimental result	Error rate
$t = 30^\circ, s = 14^\circ$	52.5°	51°	2.9%
$t = 40^\circ, s = 3^\circ$ (with a concentrator)	46.98°	48.23°	2.6%
$t = 45.19^\circ, s = 14^\circ$	37.51°	35.74°	5%

of the FLS. To verify the predicted slope, we compared the experimental results with the changing sonar configuration. As shown in Table 1, it is proven that the predicted value is reliable and similar to the slope of the pointclouds generated in the experiment. If a perpendicularly protruded object is given, then the front slope can be modified by detecting the predicted slope. The single sonar method, however, has still limitations for inclined objects, and we propose using an additional sonar to overcome this limitation.

3 Sensor fusion of two sonar devices

The FLS on an AUV can generate rough 3D pointclouds of the seabed using additional altitude data from the DVL and acoustic beam geometry, but the pointclouds have a front slope in the front area of the generated points of a protruded object. Although the slope is predictable, the real slope is unknown. In the single sonar method, only one additional range data and its incident angle are used. By means of increasing the additional information, the accuracy of the generated pointclouds can be improved. For additional information, we used mechanical scanning PS. The PS provides the range data and its angular position, providing abundant information. To correct the front slope, we must determine the vertical sectional information of an unknown object on a seabed, which is provided by the PS. For additional sonars, any sonar can be used to obtain vertical information such as an additional FLS. However, the PS scans a longer range than the FLS. The longer scanning range of the PS provides less drift information than that of a short scanning range sonar, which is a merit for data association and for expanding the simultaneous localization and mapping (SLAM) framework as a future work.

3.1 Sonar configuration

The PS we used originally scans a 2D horizontal plane by rotating a transducer head at pre-set angular increments and insonifies a pan-shaped beam that has a narrow horizontal beam spreading angle and a wide vertical beam spreading angle. The horizontal beam spreading angle is 1.8° , and the vertical beam spreading angle is 20° with the range of 10 m. The scanning speed can be set from 0.3° per step to 2.4° per step with 0.3° increments. The scanning area is set by limiting the rotating angular head position to the preset value. The limit of the rotating angular head position determines the scanning sector. Unlike multibeam sonars, the secondary PS requires time to obtain the complete data of the scanning, because the PS generates a complete data by rotating its transducer head mechanically. Therefore, for each of the resulting returns from the rotating transducer, each angular position should be compensated for by the motion of the AUV. In this study, the PS was installed by laying it down on its side to scan the vertical profile of the front area of the AUV (Fig. 8).

The PS is was installed differently, i.e., rotated 90° with respect to the roll direction (placed on its side), to obtain the vertical section information. The features of the obtained data from the two sonar sensors are complementary, and the data from the one sonar sensor enhances the data from the other sonar sensor (Fig. 9); one sonar sensor, i.e., the FLS, scans the horizontal information with a high resolution, and the other sonar sensor scans the vertical profile of the frontal

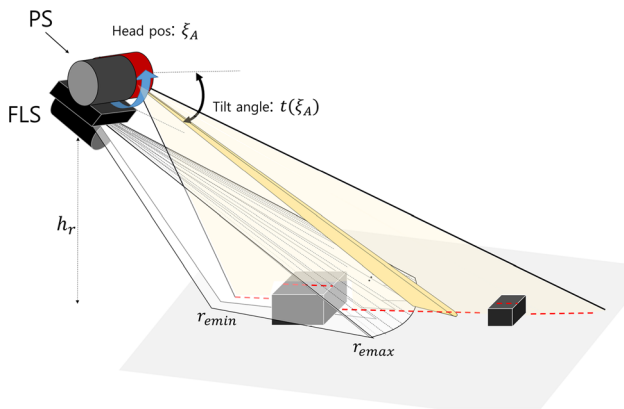


Fig. 8 Acoustic beam geometry of the PS

area of the AUV with a low resolution. In this section, we present a method to improve the generated pointclouds using the data fusion of FLS and PS.

3.2 Submap generation and sectional slicing

To correct the front slope, we require the real vertical sectional information of an unknown object. The FLS provides high-resolution sonar images with less accurate vertical sectional information. Meanwhile, the PS provides vertical sectional information with a narrow horizontal view. The pointclouds roughly generated by FLS were corrected and enhanced by combining data from PS (Fig. 10). The data fusion of the two different sonar sensors was performed via a submap-based vertical sectional slicing line feature extraction method. First, the size of the submap and the width of the sectional slice were determined according to the speed and altitude of the AUV, and the two local submaps were generated, which consist of points generated on the basis of the FLS and PS measurements. The generated submap was divided into vertical sectional slices of predetermined width, and it was investigated as to whether an object was presented or not in the sliced section. A vertical sliced section containing an object is called an occupied sectional slice. The size of the submap depends on the speed of the AUV and sonar configuration. Given that the AUV moves at speeds from 0.1 to 0.2 m/s and the required scan time of the PS to obtain a vertical profile is around 5 seconds, the submap size is determined as 2 m, because at least double scanning is required to obtain a reliable vertical profile. The width of the sectional slicing depends on the altitude of the AUV and sonar configuration. The number of points in a sectional slice should be sufficient for line feature extraction. Given that the FLS consists of 96 transducers and the altitude is approximately 2 m, the combination of four transducer covers 0.08 m. For every sectional slice, RANSAC-based line feature extraction was applied, and points in each sectional slice were clustered as an object

and seabed part based on the slope of the line features. The points were classified as an object exhibiting a front slope, and for their correction, real sectional information with low uncertainties was provided by the PS. To estimate the real slope of an object in the local point map of the PS, a principal component analysis (PCA) and voting were used for obtaining the most relevant line feature. The algorithm first clustered the points using PCA and then sought a line feature with the largest number of inliers, except for lines representing the seabed. Its slope was used to correct the front slope in the local map of the FLS. The vertical information in the local map of the PS is reliable but extremely narrow, which is enhanced by the FLS data. The occupied sectional slices in the local map of the FLS were used to enhance the PS data. On the basis of the occupied sectional slice, the local map of the PS was padded. Consequently, the two local maps of both sonars were enhanced, and registered into a global map.

3.3 Line-feature extraction and clustering

The generated pointcloud through the FLS include of surfaces, and the 3D shapes of the objects on the seabed vary. Without prior information, a 3D shape cannot be easily specified in the generated pointclouds. Therefore, we used vertical sectional information in 2D rather than 3D shape matching and extracted the line features. Let the local maps of the FLS and PS be $L_D = \{l_{D,i} | i \in 1 \dots N\}$ and $L_A = \{l_{A,i} | i \in 1 \dots N\}$, respectively. The associated submap is defined as $M = \{m_i | i \in 1 \dots N\}$, which is generated every 2 m. The local map of the FLS exhibited a relatively wide and high resolution, but it also exhibited a front slope caused by its vertical acoustic beam spreading angle width. Meanwhile, the PS map was extremely narrow and of low resolution. To utilize the profiling data, the local map of the FLS was divided into vertical sectional slices as $l_{D,i} = \{s_j | j \in 1 \dots k\}$. The sectional slices contained half-by-half overlapping areas with a width of 0.08 m to obtain sufficient points in each slice and to increase the resolution.

Given that a local map of the FLS $l_{D,i}$ and sectional slice $s_{(j=1:k)}$ were generated, clustering was subsequently applied to extract points representing the object. Clustering is a split and merge algorithm based on PCA (Gerogiannis et al. 2011). The goal of clustering is to divide the vertical sectional data into the seabed and objects, which describes the points using the principal axis. Therefore, given the points $\mathbf{x} = \{x_1, \dots, x_n\}, x_i \in \mathbb{R}^2$, the objective function of the PCA-based algorithm is as follows:

$$\text{Find } s \text{ to minimize } \Delta = \sum_{\mathbf{x} \in s_i} d(\mathbf{x}, \lambda_1 e_1), \quad (22)$$

where $s = \{s_1, \dots, s_k\}$ is the clustering set; λ_1 is the larger eigenvalue of $\mathbf{x} \in s_i$, such that $\lambda_1 > \lambda_2$; and e_1 is the eigen-

Fig. 9 Fusion based 3D mapping of the two sonar devices. The 3D reconstruction becomes deterministic with the combination of the data of the two devices

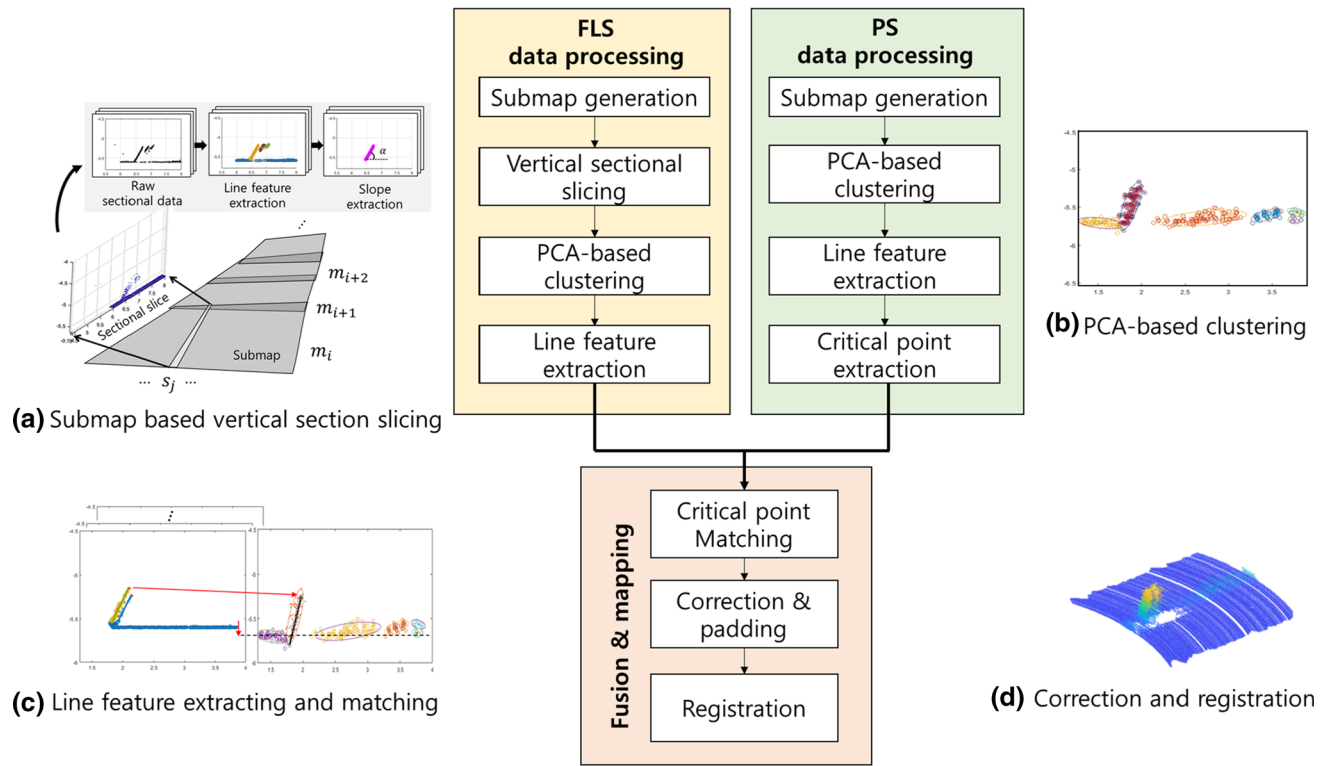
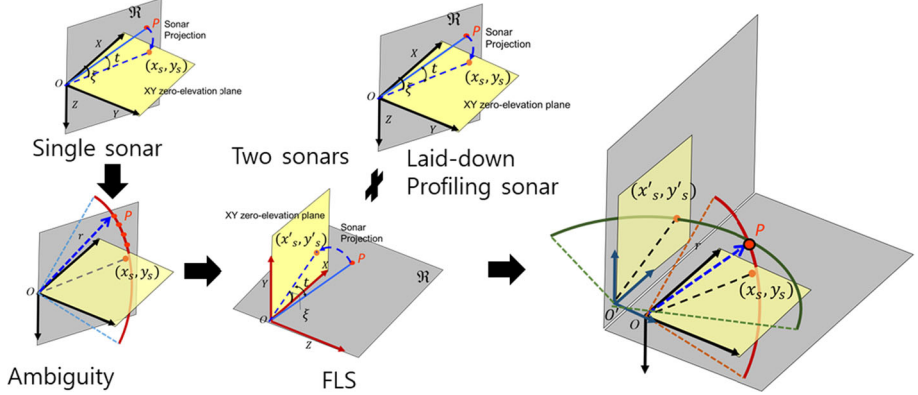


Fig. 10 Flow chart of the proposed 3D mapping method. Successive data were acquired from the two sonar sensors, and two submaps were generated. **a** Submap of the FLS sliced for vertical sectional information, and **b** point in the submaps clustered as a seabed and objects. In

both submaps, the line features were extracted, and critical points that indicate the object location were estimated. **c** Two submaps matched based on the critical point and corrected by the compensating information. **d** Associated map registered to the global map

vector corresponding to λ_1 . $d(\mathbf{x}, \lambda_1 e_1)$ is the perpendicular distance of a point in a clustering set to its principal axis $\lambda_1 e_1$. The updating of the center of the cluster is continued by verifying the eigenvalues to the predetermined thresholds, which is described as

$$\text{if } T_1 < \lambda_{t,2} < T_2 \text{ then } \mu_{t+1,1} = \mu_t + \sqrt{\lambda_{t,1}} e_{t,1}, \quad (23)$$

$$\mu_{t+1,2} = \mu_t - \sqrt{\lambda_{t,1}} e_{t,1}, \quad (24)$$

$$\text{else if } \lambda_{t,2} > T_2 \text{ then } \mu_{t+1,1} = \mu_t + \sqrt{\lambda_{t,2}} e_{t,2}, \quad (25)$$

$$\mu_{t+1,2} = \mu_t - \sqrt{\lambda_{t,2}} e_{t,2}, \quad (26)$$

where T_1 is a threshold to split in the largest principal axis, and T_2 is a threshold to split in the smallest principal axis. The merging process is conducted by considering linearity. Given that $s_i, s_j \in \mathbf{s}$, $i \neq j$, let $\lambda'_{i,1}$ be the largest eigenvalue such that the covariance matrix of $s_{i,j} = s_i \cup s_j$. Then the merge algorithm proceeds when the following inequalities are satisfied:

$$\text{if } \|\mu_i - \mu_j\| < 2(\sqrt{\lambda_{i,1}} + \sqrt{\lambda_{j,1}}) \text{ and } 2\sqrt{\lambda'_{i,2}} < T_1 T_3, \quad (27)$$

$$\text{then, } s_i = s_{i,j}, \quad (28)$$

where T_3 is a positive constant.

After the clustering process, the clusters labeled as objects are represented by line features. The line features were extracted by RANSAC based multiline extraction. Two points were randomly selected, and the model parameters were estimated. The model to be estimated is as follows:

$$\sin(\alpha')(\mathbf{x} - s_x) = \cos(\alpha')(\mathbf{z} - s_z), \quad (29)$$

where s_x and s_z are the center of masses of the selected points, and α' is the slope of the estimated line. The model parameters are calculated by the probabilistic approach in Arras and Siegwart (1998) as follows:

$$s_x = \frac{\sum w_i x_i}{\sum w_i}, s_z = \frac{\sum w_i z_i}{\sum w_i}, \quad (30)$$

$$\tan(2\alpha') = \frac{-2 \sum w_i (s_z - z_i)(s_x - x_i)}{\sum w_i [(s_z - z_i)^2 - (s_x - x_i)^2]}, \quad (31)$$

where w_i is the measurement uncertainty. The calculated parameters were verified by estimating the number of points sufficiently close to the predefined tolerance ϵ , and the close points are labeled as inliers. If the number of inliers does not exceed the preset threshold η , then the model parameters are re-estimated. Otherwise, the model is adopted, and the inliers are excluded from s_j . If the number of the remaining points in s_j does not exceed a predetermined size S , then the process is terminated. Otherwise, the process repeats until the condition is satisfied. If the model is adopted and is satisfied within the criterion, then the inliers are classified as a seabed. Otherwise, the inliers are classified as an object. The criteria are $\alpha' < \Theta_{thr}$ and $|\cos(\alpha')(z - s_z) - \sin(\alpha')(x - s_x) - h_r| < 2\sigma_r$, where σ_r is the uncertainty in the range measurement of the FLS. Θ_{thr} denotes a threshold that is represented as $\Theta_{thr} = 2 \tan^{-1} \sigma_r$. If a sectional slice s_j contains an object, then the sectional slice is labeled as an occupied sectional slice, which is used for the padding of data of the PS.

3.4 Correction of the local map of the FLS

The correspondences of the two local maps must match. First, we assume that the AUV mounting two sonar sensors exhibits good stability in roll and pitch motions by adjusting the proper center of mass and buoyancy. In addition, we assume that the drift of the dead reckoning in the submap is little, and the accuracy of the submap is sufficiently consistent (Massot-Campos et al. 2016). Our approach uses line feature extraction on the vertical sectional slice, and the data of the PS

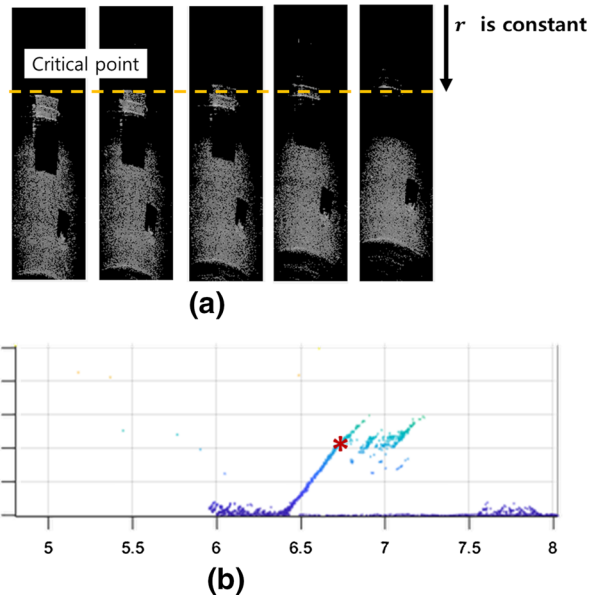


Fig. 11 Sonar image variations when approaching an object by the AUV (left) and sectional profiling of the resulting point map(right). The red star presents the critical point

have a narrow shape. Therefore, we consider the correspondence in the X-Z plane; the correspondence in the Y-plane was matched using an occupied section, which is described later. The correspondence in the X-Z plane of the two local maps matches based on the location of an object. To localize the object, the critical points were used. Let the inliers of the extracted line feature of the front part of the points represent an object in a sectional slice be $\mathbf{x}_i = \{x_i | i \in 1 \dots n\}$, $x_i \in \mathbb{R}^2$. The critical point, \mathbf{x}_c can be obtained by estimating the maximum distance from the center of mass of the inliers. On the basis of the estimated critical point of both maps, the correspondence in the X-Z plane was matched as follows:

$$\mathbf{x}_c = \operatorname{argmax}_{x_i \in \mathbf{x}_i} d(E(\mathbf{x}_i), \mathbf{x}_i), \quad (32)$$

$$\Delta p_i = \mathbf{x}_{c,A} - \mathbf{x}_{c,D}, \quad (33)$$

$$s'_j = R(s_j + \Delta p_i) \quad (34)$$

where operator E denotes the average, and $\mathbf{x}_{c,A}$ and $\mathbf{x}_{c,D}$ are the critical points of the local maps of the PS and FLS, respectively. R is the rotation matrix that is calculated by comparing the seabed slope between the two sonar sensors' data (Fig. 11).

The points classified as object had a sloping shape in the front part owing to the ambiguity of the acoustic beam, and the slope was estimated through the line-feature extraction. To modify the error in the slope, the real value of the slope should be estimated. Because the PS has a vertical beam spreading angle and the sonar equipped AUV moves, the data from the PS contain ambiguities and uncertainties. Therefore, we cannot measure the exact value of an object; instead, we

used the less erroneous estimated value of the object. We estimated the slope of the object from the local map of the PS using the same method described above. A line extraction method on $l_{A,i}$ after clustering of the selected line slope, α_{est} , was used to correct the front slope by $\Delta\alpha = \alpha_{est} - \bar{\alpha}'$ where $\bar{\alpha}'$ is the front slope estimated by averaging the values along the sectional slices. The points composing a front slope were corrected by the following equations

$$\begin{bmatrix} x'_j \\ y'_j \\ z'_j \end{bmatrix} = \begin{bmatrix} \cos \Delta\alpha & 0 & -\sin \Delta\alpha \\ 0 & 1 & 0 \\ \sin \Delta\alpha & 0 & \cos^2 \Delta\alpha \end{bmatrix} \begin{bmatrix} x_j - \bar{x}_c \\ y_j - \bar{y}_c \\ z_j - \bar{z}_c \end{bmatrix} + \begin{bmatrix} \bar{x}_c \\ \bar{y}_c \\ \bar{z}_c \end{bmatrix}, \quad (35)$$

where $[\bar{x}_c, \bar{y}_c, \bar{z}_c]^T$ is the object location that is the critical point, and $[\bar{x}_j, \bar{y}_j, \bar{z}_j]^T$ are the points composing the front slope.

3.5 Correction of the local map of the PS

The narrow data of the PS were enhanced by the FLS data. The PS data are more reliable vertically than the FLS data but are extremely narrow horizontally. Although the FLS exhibits ambiguity in vertical information, it provides high-resolution and reliable horizontal information. The previous section describes that the ambiguity of the FLS data is corrected by the PS data. This section addresses a method to pad the PS data using the horizontal information of the FLS. The horizontal information of the FLS was extracted by clustering the line feature in the sectional slice. The sectional slices that exhibit the line feature of the object are labeled as an occupied sectional slice. The enhancement in the local map of the PS was conducted by duplicating the data of the PS at the occupied sectional slices, which is called padding, because the occupied sectional slices are typically adjacent. Next, the padded data were modified on the basis of the critical point of each occupied section. The critical point contains the height and location information. This process is akin to a carving behavior. The padded data were carved by a critical point along the sectional slice. The corrected maps are associated to the submap, and the submap was registered into the global map.

$$m_i = l'_{D,i} \cup l'_{A,i} \quad (36)$$

3.6 Error analysis

The quality of the generated pointclouds was evaluated by estimating the errors in the height, width, front slope and volume. The volume of the reconstructed object was simplified as shown in Fig. 12. The volume in red color represents the volumetric error caused by the front slope. The volume of

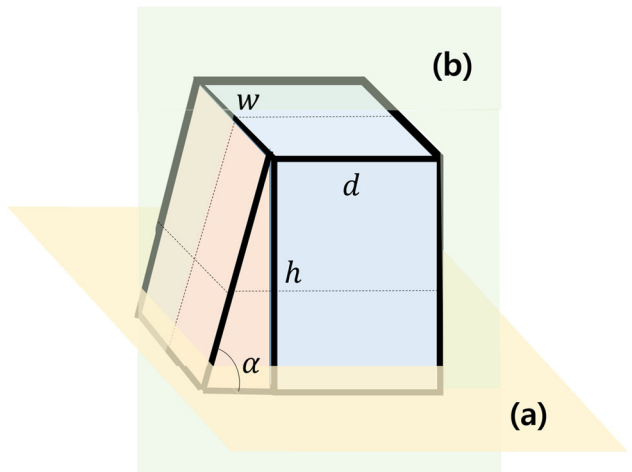


Fig. 12 Volumetric representation of the generated pointclouds of a protruded object on the seabed (the red color is the volumetric error caused by the front slope)

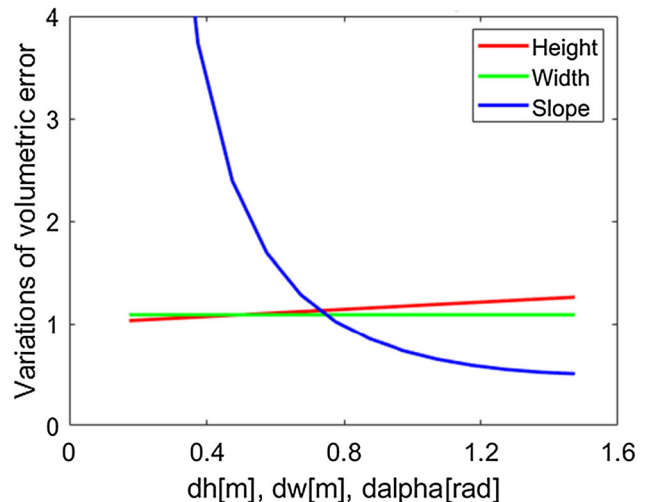


Fig. 13 Volumetric error variation with the changing height, width, and slope

the generated pointclouds can be presented by Eq. 37.

$$V = \frac{h^2 w}{2 \tan \alpha} + d w h \quad (37)$$

$$\begin{aligned} \Delta V = & \left(\frac{h w}{\tan \alpha} + w \right) \Delta h + \left(\frac{h^2}{2 \tan \alpha} + h \right) \Delta w \\ & + \left(\frac{h^2 w (\tan^2 \alpha + 1)}{2 \tan^2 \alpha} \right) \Delta \alpha \end{aligned} \quad (38)$$

To compare the volumetric variations by changing the parameters, we applied partial derivatives to Eq. 37, and obtained Eq. 38. Figure 13 shows the variations in the volumetric errors with respect to the height, width, and slope. The slope primarily affects the variation in the volumetric error. Therefore, we evaluated the quality of the generated point-

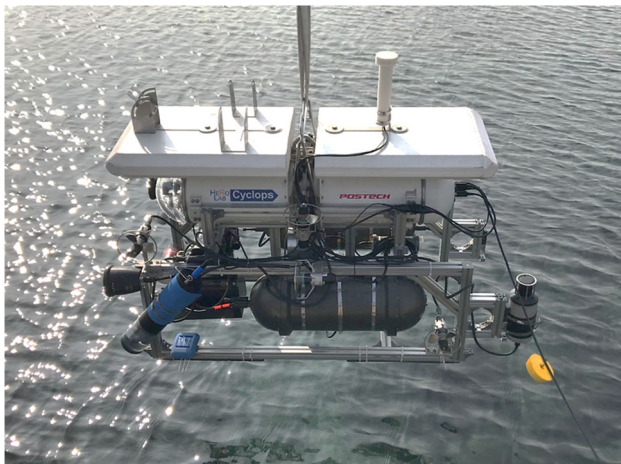


Fig. 14 Hovering type AUV *Cyclops* in the field test

clouds by comparing the slope errors. To quantify the errors caused by the slope, we compared the overlapping projection area between the pointclouds generated by the proposed method and the ground truth in the bottom and lateral faces using the intersection over union (IOU). As shown in Fig. 37, the pointclouds are projected into the 2D plane in the bottom (a) and lateral sides (b). The projected area was compared with the ground truth, which was generated from the 3D CAD model of objects used in the experiments. The IOU is calculated as follows:

$$\text{IOU} = \frac{A_{proj} \cap A_{gt}}{A_{proj} \cup A_{gt}}, \quad (39)$$

where A_{proj} is the area of the generated pointclouds in the 2D plane projected into either the X-Y or X-Z plane, and A_{gt} is the area of the ground truth object.

4 Experiment

4.1 Experimental setup

We applied the proposed method on experiments using an AUV named *Cyclops* (Fig. 14) developed at Pohang University of Science and Technology (POSTECH) (Pyo et al. 2015; Joe et al. 2014). *Cyclops* is a hovering-type AUV comprising eight thrusters: two for surge, four for sway, and two for heave motions. The specifications of the vehicle are presented in Table 2. The X-Y positions of the AUV were obtained using the DVL, and the Z position was gathered using a pressuremeter. The angular orientation was measured using a fiber-optic gyroscope. The sensor system were composed of the FLS, called DIDSON, PS, laser and optical cameras, and the sensor data were synchronized and merged with the position data in the predetermined period.

Table 2 Specification of the hovering type AUV *cyclops*

Weight	210 kg in air
Depth rating	100 m
Propulsion	8 thrusters(475 W)
Max. speed	2 knots
Power source	24 VDC (600 Wh Li-Po battery x 2
Computer system	PC-104 x 2
Sensors	Forward-looking sonar(1.1MHz/1.8MHz) Profiling sonar (675 kHz/ 1MHz) Digital pressure transducer Doppler velocity log (1.2 MHz) Still camera (10 Mpixels) Fiber optic gyro Video camera

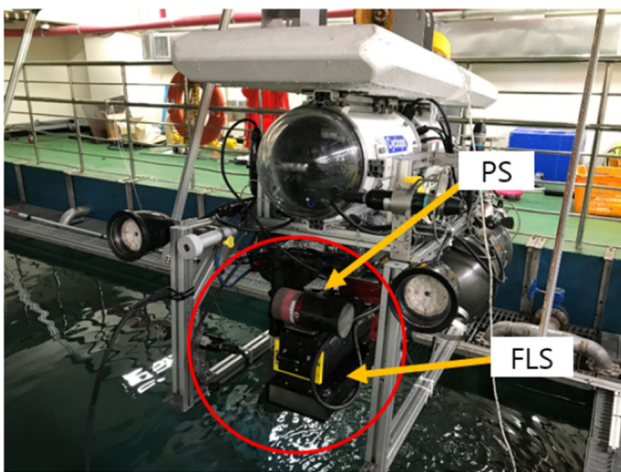
The experiments were carried out in an indoor water tank. For sonar installations, the FLS was mounted on a pan-tilt rotator, and the PS was fixed at the top of the FLS by rotating it on its side as shown in Fig. 13. The configurations of the sonars were varied in four different settings to verify the quality of the generated pointclouds with changing sonar configurations. For the first configuration of the sonars, the FLS was set to exhibit a tilt angle of 45°, a window length of 5 m, a window start of 0.42 m, and a sonar gain of 40. The PS was set to exhibit a range of 10 m, a sonar gain of 30, a scanning sector of 45°, and a stepsize of 1.2° per step. For the second configuration, the sonar tilt angle was changed to 30°. For the third configuration, we used a sonar concentrator to change the acoustic beam-spreading angle, which decreased the beam-spreading angle up to 3°, and the sonar tilt angle was 40°.

To test the proposed algorithm, we deployed five different objects, and conducted three experiments. For the first experiment, we used three objects: a concrete brick, an aluminum cylinder, and a plastic basket. Then, the sonars were set according to the first configuration. For the second experiment, we added two objects: a tilted trapezoid-shaped wood panel and a sphere-shaped plastic container, and we used the second sonar configuration. For the last experiment, the five objects were deployed with the third sonar configuration. The tilted wood panel was a difficult to reconstruct, because it was tilted and has a trapezoid shape. A simple method that corrects the front slope without the real value of the slope cannot retain its original slope. In addition, the PS cannot describe the trapezoidal shape of the wood panel. Therefore, the wood panel is an important object to verify the proposed method. The proposed method was demonstrated by reconstructing five different objects in a rectilinear scan.

The AUV scanned slowly along with the preset waypoints with an altitude of 2.61 m. Both sonars acquired data at a 10-

Table 3 Experimental setup for the three experiments

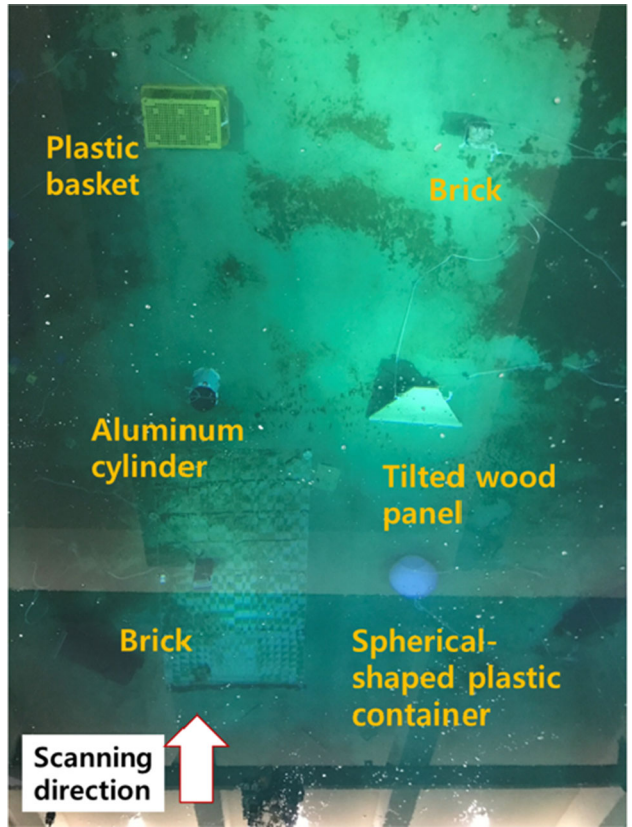
		Exp 1	Exp 2	Exp 3
FLS	Window length	5	5	5
	Window Start	0.42	0.42	0.42
	Gain	40	40	40
	Tilt angle	45	30	40
	Beam spreading angle	29° x 14°	29° x 14°	29° x 3°
PS	Range	10	10	10
	Gain	30	30	30
	Sector	45	60	60
	Step size	1.2	1.2	1.2

**Fig. 15** AUV *Cyclops* and sonar installations (red circle)

Hz frequency. The position data of the AUV were associated with the sonar data at a frequency of 10 Hz (Table 3, Figs. 15, 16).

4.2 Results of the indoor tank test

The results from the tank test are presented in Fig. 17. The first left column indicates the real objects used in the test and their sizes. The second column presents the results generated by the FLS only. The generated pointclouds are represented through a triangle mesh and are properly cropped for analyzing their quality. The black lines in each map represent the real objects. The results of the proposed method are presented in the third column. The fourth column shows the top view of the results through the FLS only, and the last column shows the top view of the results from the proposed method, demonstrating the improvement in the frontal shapes of the reconstructed results. For the results of the FLS only, the front slopes are shown; however, for the results of the proposed method, the slopes were improved. The tilted wood panel retained its slope and trapezoidal shape. For the cylin-

**Fig. 16** Overview of the indoor tanktest: six objects deployed

drical and sphere-shaped container, the resulting pointclouds maintained their rounded front shapes.

For a quantitative comparison, we measured the height, width, and slope, and calculated the volumetric errors of the generated pointclouds using Eq. 37, which are presented in Tables 4 and 5. The slope errors and volumetric errors were improved; for the brick, the slope and volumetric error rate were improved by 32.9 % and 7.8 % on average, respectively; for the aluminum cylinder, 45.3 % and 3.4 %; for the basket, 38.6 % and 7.6 %; for the wood panel, 1.5 % and 0.7 %; for the spherical-shaped container, 28.1 % and 13.2 %, respectively. For experiment 3, we used a concentrator to adjust the vertical beam-spreading angle to 3°. It was expected that the smaller beam-spreading angle would result in better results with smaller uncertainties. However, the results of the proposed method without the concentrator presented lower error rates compared with the results through the FLS only with the concentrator.

Table 6 shows the improved IOU values of the proposed method in comparison with the FLS only method. The proposed method obtained better IOU values with the brick by 18.5 % on average; with the cylinder by 24.4 %; with the basket by 10.8 %; with the wood panel by 6.8 %; with the spherical-shaped container by 13.5 %. These results demonstrated that the proposed method showed good performance

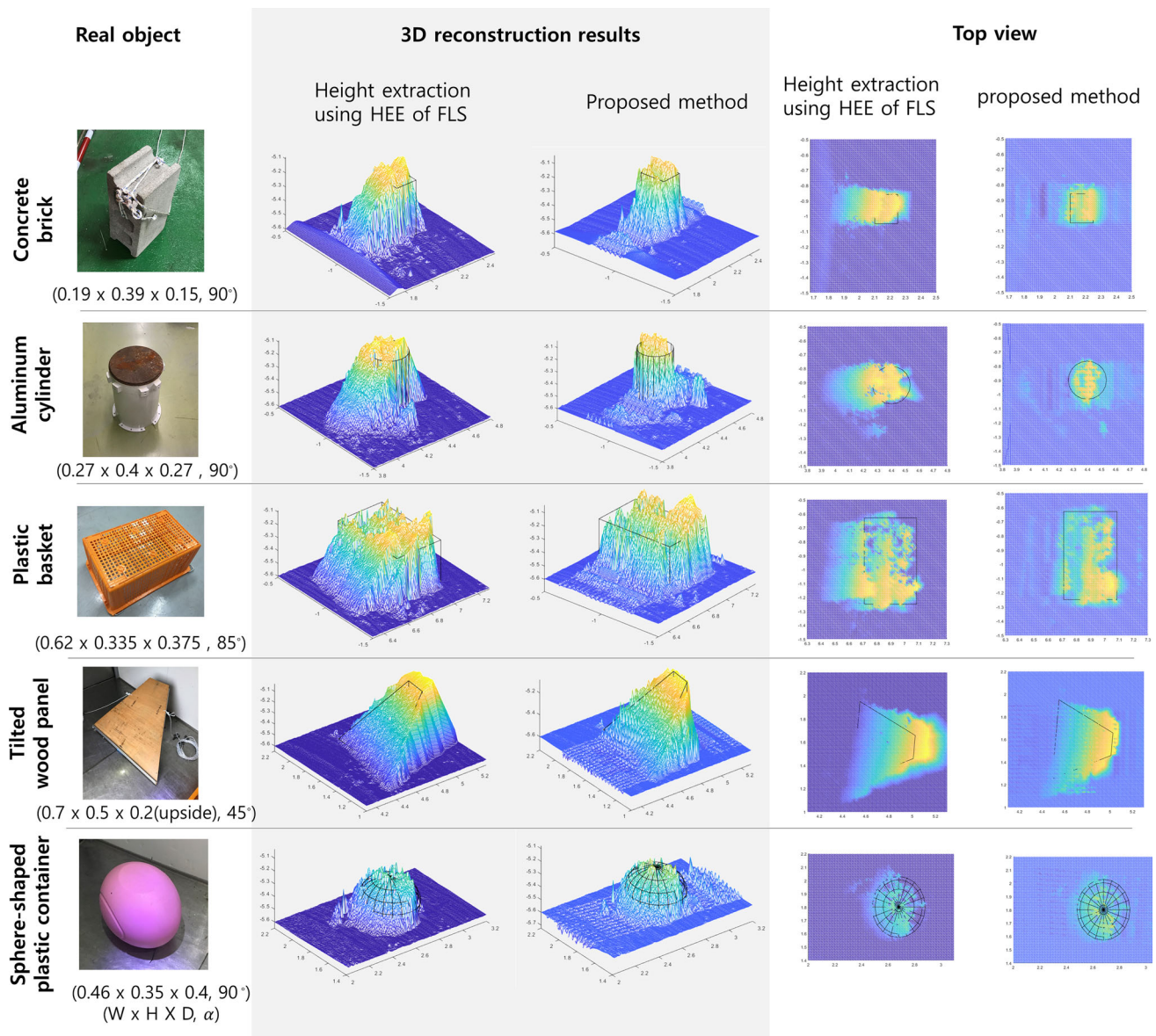


Fig. 17 Result comparison between the corrected points and real objects. The first left column presents the real objects; the second column presents the results generated by the FLS-only method; the third column presents the results generated by the proposed method; the

fourth column is the top side views of the results from the single-sonar method; the last column is the top view of the results of the proposed method. The black lines describe the sizes of the corresponding real objects

Table 4 Comparison of slope errors of the single sonar and the proposed method in each experiment

	Exp. 1		Exp. 2		Exp. 3	
	Single	Proposed	Single	Proposed	Single	Proposed
Brick	0.6029	0.2049	0.4298	0.1172	0.4599	0.1827
Cylinder	0.6029	0.0420	0.4298	0.0427	0.4599	0.0499
Basket	0.5795	0.1959	0.3963	0.0322	0.4281	0.0182
Wood panel	—	—	0.0790	0.0351	0.0975	0.1109
Spherical-shaped Container	—	—	0.4786	0.0539	0.4704	0.3338

Table 5 Comparison of volumetric errors of the single sonar and the proposed method in each experiment

		Exp. 1		Exp. 2		Exp. 3	
		Single	Proposed	Single	Proposed	Single	Proposed
	Brick	0.1000	0.0189	0.1141	0.0215	0.0910	0.0311
	Cylinder	0.0674	0.0284	0.0681	0.0297	0.0393	0.0138
	Basket	0.2611	0.1223	0.0731	0.0253	0.0863	0.0461
	Wood panel	—	—	0.1034	0.0931	0.0688	0.0639
	Spherical-shaped Container	—	—	0.1752	0.0537	0.1764	0.0331

Table 6 Comparison of IOU of the single sonar and the proposed method in each experiment

		Exp. 1		Exp. 2		Exp. 3	
		Single	Proposed	Single	Proposed	Single	Proposed
Brick	Bottom	0.2912	0.6087	0.2597	0.4160	0.4892	0.6259
	Lateral	0.3560	0.5876	0.3575	0.4943	0.4683	0.6017
Cylinder	Bottom	0.1943	0.5716	0.3146	0.5677	0.3699	0.6533
	Lateral	0.3206	0.4047	0.3524	0.6958	0.4141	0.5382
Basket	Bottom	0.4157	0.6881	0.4733	0.5873	0.5802	0.6322
	Lateral	0.3359	0.4868	0.5868	0.6030	0.5896	0.6310
Wood panel	Bottom	—	—	0.6062	0.6697	0.5740	0.7420
	Lateral	—	—	0.6381	0.6206	0.5146	0.7083
Spherical-shaped container	Bottom	—	—	0.3965	0.6361	0.4610	0.6029
	Lateral	—	—	0.4995	0.7408	0.5117	0.7066

in a one-way rectilinear scanning mission. In addition, the results of the tilted wood panel were similar in the FLS only and proposed methods.

4.3 Field experiment at sea

We conducted a field test using the same AUV and tested the proposed method at sea (Fig. 18). The AUV was launched to investigate the conditions of the mooring rope of a floating deck and to survey environments involving seaweeds and marine litters in the coastal area of Pohang in South Korea. The test spot was located inside a harbor, and crossing mooring ropes were used to hold the floating deck in the middle of the test spot. For the sonar setup, we used the same installation with the tank test, and the detailed sonar configurations are shown in Table 7. To evaluate the quality of the proposed method in the sea, we deployed reference objects such as the aluminum cylinder and concrete brick used in the tank test, because there was neither a prior map nor a ground truth. The material of the bottom and surrounding environments varies depending on the test spot, which causes different conditions in the quality of the sonar data. The backscattering by background differs from that of the indoor tank test. Therefore, the aluminum cylinder was located on an area with few sea-



Fig. 18 AUV *Cyclops* in the seabed survey

weeds, and the concrete brick was located on a sandy area (Fig. 19).

The AUV was surveyed for approximately one hour, and the results of the seatrial are presented in Fig. 20. The submap was generated every 2 m or when the heading changed significantly. We dismissed the data corresponding to when the AUV was in the yawing motion, because the proposed method is optimized for rectilinear one-way surge motion. The trajectories captured in the sea trial are presented in

Table 7 Experimental setup for seatrial

	Parameters	Values
FLS	Window length	5
	Window Start	0.83
	Gain	25
	Tilt angle	25
	Beam spreading angle	29 x 14
PS	Range	10
	Gain	25
	Sector	60
	Step size	1.2

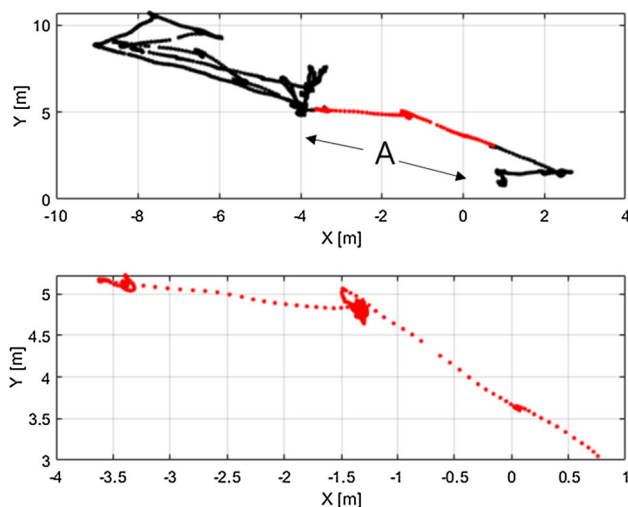
**Fig. 19** AUV trajectories during sea trial (top) and interval “A” (bottom)

Fig. 19. At the beginning of the test, the AUV passed over the reference objects. This interval was marked by a red dot and called “interval A”. The AUV in interval A scanned the reference objects, and the results are presented in Fig. 21. Object B is the aluminum cylinder, and object C is the concrete brick. To verify the quality of the 3D reconstruction of the reference object, Fig. 21b shows a magnified view. The black lines describe the size of the objects, and the mea-

sured height and width of the concrete brick were 0.4475 m and 0.2202 m, respectively. The error rates of the height and width were 15 % and 16 %, respectively. For the aluminum cylinder, the height and width are 0.4471 m, and 0.2572 m, and the error rates were 12 % and 5 %, respectively. Consequently, although many seaweeds appeared on the seabed of the test spot, the AUV could scan the reference objects.

5 Conclusion

Herein, we presented a 3D mapping method in a one-way rectilinear scanning using an AUV equipped with an FLS and a PS. As 3D reconstruction through sonar is an ill-posed problem, additional constraints are required to be considered. Our approach is to use additional sonars that provide compensative information via data fusion. Initially, we analyzed the height extraction method using HEE proposed by Cho et al. (2017). In the single-sonar method, accuracy degradations such as front slopes occurred, and we analyzed the erroneous pattern through modeling. To improve the degradation, the 3D map generated by the FLS was refined by combining the vertical scanning information from the PS. The FLS exhibited a high resolution in the horizontal scan but had elevation information losses. Meanwhile, the PS provided a reliable vertical profile, but the obtained data were extremely narrow. The local maps obtained by each sonar were combined using the line-feature based method rather than the 3D shape matching method in a sliced 2D plane. Both data were corrected using the line-features in the vertical sectional slices. To demonstrate the proposed method, we conducted an indoor tank test and a sea trial. Consequently, we demonstrated the proposed method, and we obtained a reliable 3D map. The proposed method can optimize seabed tracking to search for small objects in an environment with limited visibility by means of deterring unnecessary hovering to obtain data in different positions. As future work, we will implement our method to the SLAM framework for consistent map generation.

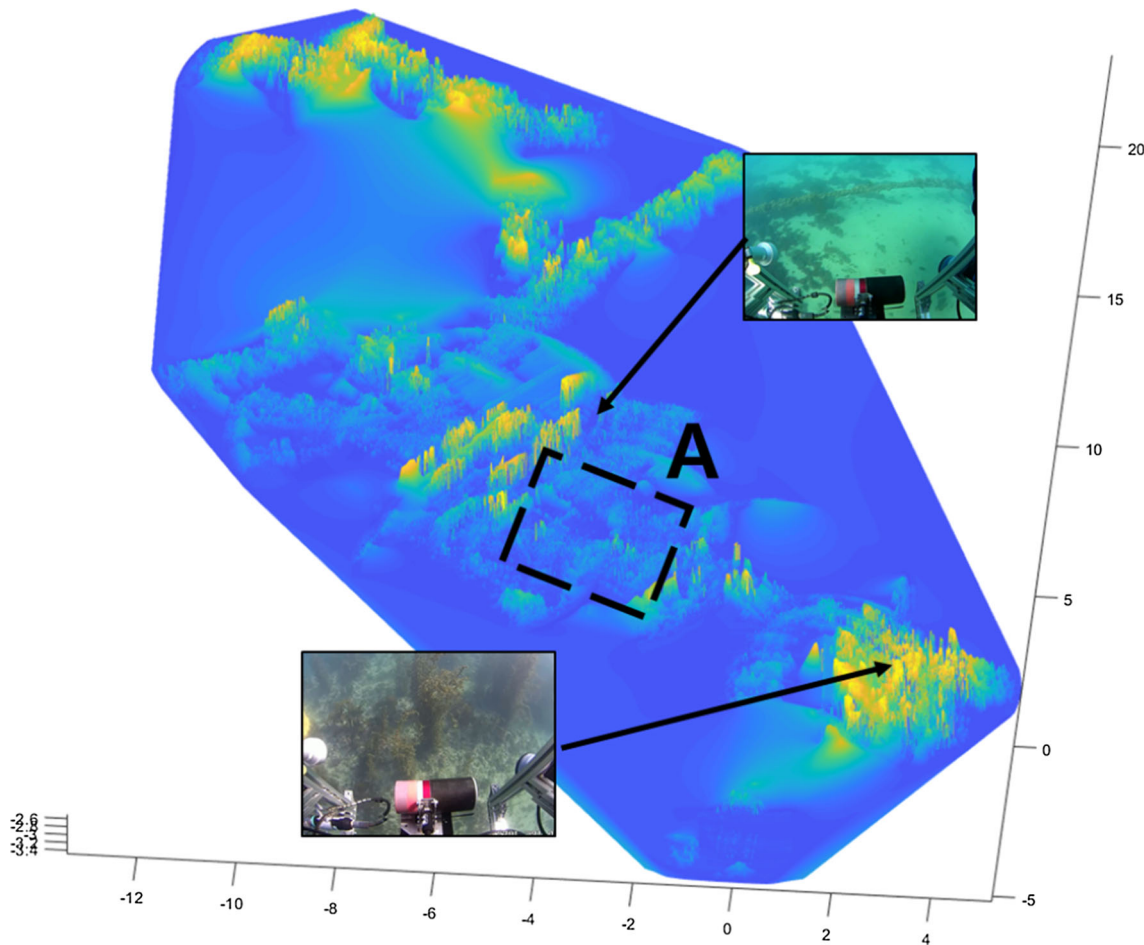


Fig. 20 3D mapping results obtained in the seatrial

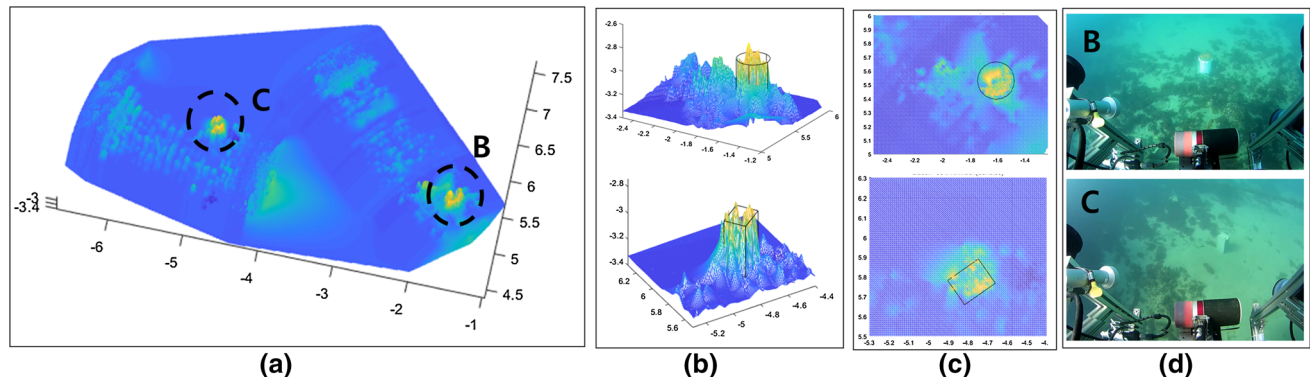


Fig. 21 a shows a magnified map of “A” in Fig. 20. “B” and “C” the reference objects (i.e., aluminum cylinder and concrete brick, respectively). b detailed map around reference objects B (upper) and C (bottom).

(c) a top view around B and C. (d) optical image corresponding to the reference objects

Acknowledgements This research was a part of the project titled ‘Gyeongbuk Sea Grant’, funded by the Ministry of Oceans and Fisheries, Korea.

References

- Arras, K. O., & Siegwart, R. Y. (1998). Feature extraction and scene interpretation for map-based navigation and map building. In: *Mobile robots 12* (Vol. 3210, pp. 42–53). International Society for Optics and Photonics.
- Aykin, M. D., & Negahdaripour, S. (2016). Three-dimensional target reconstruction from multiple 2-d forward-scan sonar views by space carving. *IEEE Journal of Oceanic Engineering*, 42(3), 574–589.
- Belcher, E., Hanot, W., & Burch, J. (2002). Dual-frequency identification sonar (DIDSON). In: *Proceedings of the 2002 international symposium on underwater technology (Cat. No. 02EX556)* (pp. 187–192). IEEE.
- Burguera, A. (2017). A novel approach to register sonar data for underwater robot localization. In: *2017 Intelligent systems conference (IntelliSys)* (pp. 1034–1043). IEEE.
- Cho, H., Kim, B., & Yu, S. C. (2017). AUV-based underwater 3-D point cloud generation using acoustic lens-based multibeam sonar. *IEEE Journal of Oceanic Engineering*, 43(4), 856–872.
- Gerogiannis, D., Nikou, C., & Likas, A. (2011). A split-and-merge framework for 2D shape summarization. In: *2011 7th international symposium on Image and Signal Processing and Analysis (ISPA)* (pp. 206–211). IEEE.
- Guerneve, T., Subr, K., & Petillot, Y. (2018). Three-dimensional reconstruction of underwater objects using wide-aperture imaging SONAR. *Journal of Field Robotics*, 35(6), 890–905.
- Hernández Bes, E., Ridao Rodríguez, P., Ribas Romagós, D., Batlle, I., & Grubulosa, J. (2009). MSISpIC: A probabilistic scan matching algorithm using a mechanical scanned imaging sonar. *Journal of physical agents*, 3(1), 3–11.
- Hurtós, N. V. (2014). Forward-looking sonar mosaicing for underwater environments (Doctoral dissertation, Ph. D. Thesis, Universitat de Girona).
- Joe, H., Kim, M., & Yu, S. C. (2014). Second-order sliding-mode controller for autonomous underwater vehicle in the presence of unknown disturbances. *Nonlinear Dynamics*, 78(1), 183–196.
- Kim, K., Intrator, N., & Neretti, N. (2004). Image registration and mosaicing of acoustic camera images. In: *Proceedings of the 4th IASTED international conference on visualization, imaging, and image processing* (pp. 713–718).
- Massot-Campos, M., Oliver, G., Bodenmann, A., & Thornton, B. (2016). Submap bathymetric SLAM using structured light in underwater environments. In: *2016 IEEE/OES Autonomous Underwater Vehicles (AUV)* (pp. 181–188). IEEE.
- Pyo, J., Cho, H., Joe, H., Ura, T., & Yu, S. C. (2015). Development of hovering type AUV “Cyclops” and its performance evaluation using image mosaicing. *Ocean Engineering*, 109, 517–530.
- Ribas, D., Ridao, P., Neira, J., & Tardos, J. D. (2006). SLAM using an imaging sonar for partially structured underwater environments. In: *2006 IEEE/RSJ international conference on intelligent robots and systems* (pp. 5040–5045). IEEE.
- Ribas, D., Ridao, P., & Neira, J. (2010). *Underwater SLAM for structured environments using an imaging sonar*. Cham: Springer.
- Teixeira, P. V., Kaess, M., Hover, F. S., & Leonard, J. J. (2016). Underwater inspection using sonar-based volumetric submaps. In: *2016 IEEE/RSJ International Conference on Intelligent Robots and Systems (IROS)* (pp. 4288–4295). IEEE.
- VanMiddlesworth, M., Kaess, M., Hover, F., & Leonard, J. J. (2015). Mapping 3d underwater environments with smoothed submaps. *Field and service robotics* (pp. 17–30). Cham: Springer.
- Walter, M. R. (2008). *Sparse Bayesian information filters for localization and mapping* (No. MIT/WHOL-2008-12). Woods Hole Oceanographic Institution MA Department of Ocean Engineering.
- Walter, M., Hover, F., & Leonard, J. (2008). SLAM for ship hull inspection using exactly sparse extended information filters. In: *2008 IEEE international conference on robotics and automation* (pp. 1463–1470). IEEE.

Publisher's Note Springer Nature remains neutral with regard to jurisdictional claims in published maps and institutional affiliations.

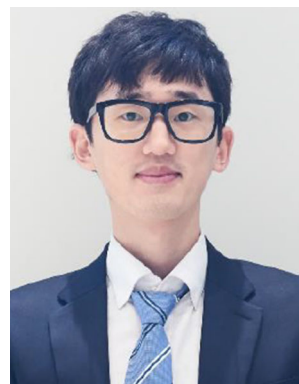


Hangil Joe

Hangil Joe received the B.S. degree in mechanical engineering in 2012 from Pusan National University, Busan, Korea, and the M.S. degree in ocean engineering in 2014 from Pohang University of Science and Technology (POSTECH), Pohang, Korea. He earned Ph.D. degree in the Department of Creative IT Engineering at POSTECH in 2019. In 2020, he joined the faculty of the Kyungpook National University, Daegu, Korea. He has been working in the areas of field and under-



Hyeonwoo Cho received the B.S. degree from the Department of Electronic, Electrical and Computer Engineering, Hanyang University, Seoul, Korea, in 2006, and Ph.D. degrees in the Department of Electronics and Electrical Engineering, Pohang University of Science and Technology, Pohang, Korea. His current research interests are in estimation theory, adaptive signal processing, and mobile robot localization.



Minsung Sung received the B.S. degree from the Department of Creative IT Engineering at Pohang University of Science and Technology, Pohang, Korea, in 2015, and is currently working toward the Ph.D. degree in the Department of Creative IT Engineering at POSTECH. His research interests include machine learning, convolution neural network, and underwater perception.



Jinwhan Kim received B.S. and M.S. degrees in Naval Architecture and Ocean Engineering from Seoul National University, Seoul, Korea, and then earned M.S. and Ph.D. degrees in Aeronautics and Astronautics from Stanford University in the United States. Kim was with Korea Institute of Machinery and Materials, and subsequently with Korea Ocean Research and Development Institute. He was also with Optimal Synthesis Inc. in California, as a research scientist. In 2010, he joined the faculty of

the Korea Advanced Institute of Science and Technology, Daejeon, Korea. He has been working in the areas of robotics and the guidance, control and estimation of dynamical systems. Kim is a member of IEEE and a senior member of AIAA.



Son-cheol Yu received the B.E. degree in naval architecture and ocean engineering from Inha University, Incheon, South Korea, in 1998 and the M.E. and Ph.D. degrees in ocean and environmental engineering from The University of Tokyo, Tokyo, Japan, in 2000 and 2003, respectively. From 2008 to 2010, he was a faculty member with the School of Mechanical Engineering, Pusan National University, Busan, Korea. Since 2010, he has been a faculty member at Pohang University of Science and Technology (POSTECH), Pohang, Korea. His research interests include autonomous underwater vehicle systems and hazardous environmental robotics.